KRONOS FUSION ENERGY

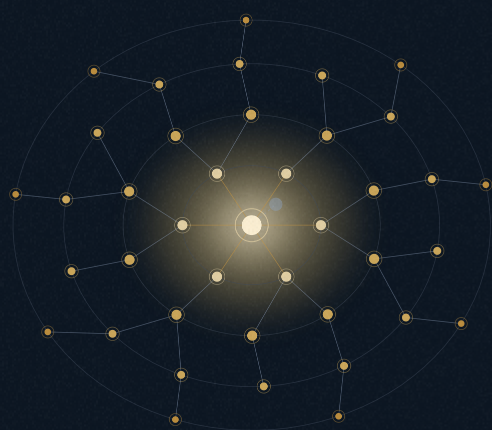

PAPER 2.95 · THE KRONOS 2026 SERIES

Quantum Chemistry Beyond DFT for Low-Activation Fusion Alloys: ADAPT-VQE Correlation Energies for Composition-of-Matter Screening with Fault-Tolerant Resource Estimates

Screening the low-activation alloys that make up a fusion reactor's plasma-facing and structural components by density-functional theory (DFT) runs into a wall: on the correlated...

Read it live — 3-D model · physics validator · film series

BY P I FORD

2026 · EDITORIAL EDITION

THE OFFICIAL RECORD

What this document is, and how to read its numbers

This is a combined editorial. It gathers, in one volume, the two design studies Kronos Fusion Energy released in 2026 — a compact spherical-tokamak tritium/helium-3 breeder and a deuterium–helium-3 tandem-mirror generator — together with the intellectual-property estate, the people, and, in the internal edition, the full commercial case. The scientific text is the same text that appears in the arXiv preprints and the journal submissions; the editorial adds the apparatus a reader needs to hold the whole program at once, and nothing in the physics is altered to fit it.

THE HONESTY STANCE IS THE ASSET

Every headline quantity carries an **evidence class** — DERIVED RECOMPUTED MEASURED REQUIREMENT — and, where a number is a modelled extrapolation rather than a demonstrated value, it is labelled as such and its downside is shown next to it. Several quantities in the underlying corpus moved after first publication; where a value has been withdrawn or restated, the record says so plainly. This is deliberate: a diligence team will find the load-bearing assumptions, so the document surfaces them first.

TWO EDITIONS

This volume is issued in two editions. The **public edition** (light) carries the physics and the design only — no dollar, price, or per-kilogram figure appears anywhere in it. The **internal edition** (dark) adds the economics, the funding architecture, and the defense-commercial analysis, and is marked *Confidential* accordingly; it is not for public distribution. Where the commercial case rests on a modelled assumption rather than a demonstrated one, it is labelled as such and its downside is shown alongside it, on the same terms as the physics.

TITLE	The Kronos Fleet — Hyperion · Aegis · MetroVolt: A Combined Design & Commercialization Study
AUTHOR	Priyanca Ford, Founder & CEO, on behalf of Kronos Fusion Energy
EDITION	2026 Combined Editorial · first issue
COMPANION WORKS	The five-paper arXiv drop — (1) Breeder, (2) Burner, (3) REBCO magnet & tape, (4) Direct Energy Conversion, (5) AI/ML/Quantum control — with matching numbered Zenodo deposits, plus the IOP journal and IAEA-FEC submissions. Patents were filed before the drop.
NAMING	Hyperion = the breeder; Aegis (defense) and MetroVolt (data-center) = one generator in two housings. Internal mode letters (D1, L) do not appear on public surfaces.
STATUS	Conceptual design & simulation study. Nothing herein is a construction commitment.

HOW TO READ THIS VOLUME

The fleet at a glance, and the way its numbers are marked

This volume opens with *Orientation*, presents the five research papers as a bound sequence, and closes with the *Apparatus*. *Foundations* sets out the three general results both machines rest on. *Paper One* is the Hyperion breeder; *Paper Two* the Aegis / MetroVolt generator; *Papers Three, Four and Five* are the enabling science — high-field REBCO magnets and tape, direct energy conversion, and the AI / ML / quantum control stack. A *Digital Twin & 3-D Model* part follows, then the *Environmental* profile. The *Economics* and levelized cost and the *Business Case* and diligence record appear in the internal edition only; the *Simulations* proof record and the Apparatus — patent portfolio, team, limitations, and sources — close both editions.

THE FLEET AT A GLANCE

	HYPERION	AEGIS	METROVOLT
Role	Strategic-isotope foundry	Defense installation power	Campus power
Machine	**Spherical tokamak**	**Tandem mirror**	**Tandem mirror**
Fuel	Deuterium–tritium	Deuterium–helium-3	Deuterium–helium-3
Delivers	Tritium · ^{3}He · 14 MeV n	Resilient installation power	Firm campus power
Physics bar	**Fusion gain only**	Closure (gates named)	Closure + lunar ^{3}He
In the fleet	Breeds the fuel	Proves the generator	Commercial destination

HOW THE NUMBERS ARE MARKED

Every headline quantity carries an evidence class — DERIVED from first principles, RECOMPUTED from raw data, MEASURED in hardware, or a REQUIREMENT yet to be met. Financial figures carry a case label and are confined to the internal (confidential) edition. Values that moved after first publication are shown as withdrawn or restated rather than quietly changed. A capability you can evaluate is one whose limits are on the page.

ABSTRACT

Quantum Chemistry Beyond DFT for Low-Activation Fusion Alloys: ADAPT-VQE Correlation Energies for Composition-of-Matter Screening with Fault-Tolerant Resource Estimates

Screening the low-activation alloys that make up a fusion reactor's plasma-facing and structural components by density-functional theory (DFT) runs into a wall: on the correlated $3d$ transition metals that constitute the family, the computed energetics depend on the exchange–correlation functional at the level of hundreds of millihartree, which is comparable to or larger than the composition differences the screen must resolve. A screen whose verdict changes with the functional is not a screen. We close that gap with an adaptive variational quantum eigensolver. We first set out the governing electronic-structure problem, the formal origin of the functional ambiguity, the well-posedness condition for a composition screen, the fermion-to-qubit mapping, and the ADAPT-VQE construction with its exact gradient-selection criterion and monotone-convergence property. We then report the frozen results of the Kronos de-risking campaign (register serial BR-SX-07): ADAPT-VQE reaches *chemical accuracy on all four $3d$-alloy fragments* (Ti, V, Cr, Fe) with a residual below $0.05\,\mathrm{mHa}$ against a correlated reference — four orders of magnitude inside the $1.6\,\mathrm{mHa}$ ($1\,\mathrm{kcal\,mol^{-1}}$) chemical-accuracy threshold and four orders of magnitude tighter than the $> 300\,\mathrm{mHa}$ DFT functional spread it replaces — using adaptively grown circuits that are 4–$14\times$ shallower in two-qubit (CNOT) count than a unitary coupled-cluster (UCCSD) ansatz at equal accuracy. An independently reproduced four-qubit proof-of-concept validates the machinery to $3.9 \times 10^{-6}\,\mathrm{Ha}$ against exact diagonalization. The results were produced on the NVIDIA GPU HPC campaign by classical statevector emulation of the quantum circuits, with plane-wave DFT and correlated quantum-chemistry references computed on the same fleet. We state the honest gate once and quantify it: this is not a claim of quantum advantage; a single-determinant ADAPT-VQE variant stalls at $24\,\mathrm{mHa}$ on the strongly multireference vacancy limit; and scaling from fragments to a full alloy or REBCO cell moves the problem into fault-tolerant quantum phase estimation, estimated at $\sim 10^9$ Toffoli gates and ~ 238 logical qubits (~ 38 days at a $1\,\mathrm{kHz}$ logical-Toffoli throughput). The deliverable is a validated, circuit-efficient electronic-structure tool for composition-of-matter screening today, with a resource-honest map of what the fault-tolerant extension will cost.

Open-access deposit (code & data, CC BY 4.0): DOI 10.5281/zenodo.22645929 · Zenodo community *kronos_fusion_energy*. Explore it live: interactive 3-D model · physics validator.

Keywords: ADAPT-VQE · variational quantum eigensolver · quantum chemistry · density-functional theory · low-activation alloy · composition of matter · fault-tolerant resource estimate

CONTENTS

Table of Contents

NOMENCLATURE

Symbols, units, and the names of things

Q	plasma (fusion) gain, P_{fus}/P_{aux}
Q_E	engineering gain, net electric out / recirculating in
H_{98}	confinement enhancement over the IPB98(y,2) scaling
Z_{eff}	effective ion charge
c_{ee}	electron–electron bremsstrahlung leading coefficient, 2.120022 (exact)
τ_E	energy confinement time
I_p	plasma current
R_0, a	major radius, minor radius
κ, δ	elongation, triangularity
β_N	normalized plasma beta (Troyon-normalized)
TBR	tritium breeding ratio
DEC	direct energy conversion
CF	plant capacity factor (availability)
FOAK / NOAK / BOAK	first / n^{th} / best of a kind
Hyperion	the ST breeder (internal: Mode D2)
Aegis	the generator, defense/installation housing (internal: Mode M)
MetroVolt	the generator, data-center housing (Mode M)

§ 1

Introduction

MATERIALS SCREENING FOR A COMPACT SPHERICAL-TOKAMAK BREEDER

Kronos Fusion Energy develops a compact, high-power-density spherical-tokamak (ST) breeder [38,39] — the Hyperion design point ($I_p = 9.66\,MA$, $Q = 3.076$, $P_{\text{fus}} = 85.04\,MW$, negative triangularity $\delta = -0.30$, on-axis field $B_0 = 8\,T$, elongation $\kappa = 2.0$, major radius $R_0 = 1.20\,m$, aspect ratio $A = 2.5$, centrepost peak field $16.84\,T$) — whose plasma-facing, structural and magnet materials must survive a hard 14 MeV neutron environment while remaining *low-activation*: no long-lived radioisotope beyond a century's half-life [1]. Meeting both constraints at once is a composition-of-matter problem: for a family of candidate alloys built from a restricted palette of $3d$ and refractory transition metals, one asks which mixture gives the best combination of melting point, ductility, phase stability and activation [35,36]. The high-entropy and reduced-activation alloy concepts that dominate the modern search [37] multiply the candidate count to the point where reliable computational ranking, not experiment, is the rate-limiting step. Kronos runs this screen as an integrated pipeline: a machine-learning interatomic-potential pre-filter, a first-principles reference, and a down-selection to activation transport [6,4,5].

THE DENSITY-FUNCTIONAL-THEORY WALL

The workhorse of the first-principles layer is density-functional theory (DFT) [26,27]. DFT is exact in principle but approximate in practice, because the exchange–correlation functional is unknown and must be modelled [28]. On the open-shell $3d$ transition metals at the heart of the low-activation family, the d-electrons carry strong static and dynamic correlation that the standard local, semi-local and hybrid functionals treat only approximately and, crucially, *inconsistently with one another* [31,32]. Corrections such as DFT+U [29,30] help but introduce their own empirical parameter. In the Kronos campaign the total-energy spread across the functionals relevant to these fragments exceeds $300\,\text{mHa}$ (register serial BR-SX-07 [1]). Because a composition screen turns on energy *differences* smaller than that spread, the functional choice — not the chemistry — can decide the ranking. This is the DFT wall: the method's own uncertainty is larger than the signal it is asked to resolve.

QUANTUM ELECTRONIC STRUCTURE AND PRIOR ART

Quantum computers offer a route past this wall because the ground state of the electronic Hamiltonian can, in principle, be obtained without any exchange–correlation model [17,16]. Two families of algorithm exist. Quantum phase estimation (QPE) extracts eigenvalues to arbitrary precision but requires a fault-tolerant machine and deep, coherent circuits [17,21]; modern resource analyses of chemically relevant systems put the cost at 10^9–10^{15} Toffoli gates and hundreds to thousands of logical qubits [22,23,24,25]. The variational quantum eigensolver (VQE) [8] is the near-term alternative, well suited to the noisy intermediate-scale quantum (NISQ) era: a parameterized circuit is optimized classically to minimize the energy expectation, trading circuit depth for a classical outer loop. VQE has been demonstrated on small molecules on hardware [12,11] and reviewed extensively [15,16]. Its practical bottleneck is circuit depth: the standard unitary coupled-cluster (UCCSD) ansatz [13,33] produces circuits too deep for near-term devices and, in the strongly correlated regime, can itself struggle [14]. The adaptive derivative-assembled pseudo-Trotter VQE (ADAPT-VQE) [9,10] addresses depth directly, growing the ansatz operator by operator so that only the excitations the specific system needs are included. Barren-plateau trainability [18] and fermion-to-qubit encoding [19,20] complete the near-term toolbox.

GAP AND CONTRIBUTION

Prior art establishes that VQE can reach chemical accuracy on small molecules and that QPE can, in the fault-tolerant limit, solve larger ones. What has not been shown for a fusion-materials program is a *decision-grade* statement: a quantitative demonstration that an adaptive VQE resolves the exact composition question DFT leaves ambiguous on the correlated $3d$-alloy fragments, together with a resource-honest map of the gap between that fragment-scale capability and a full-cell calculation. This paper supplies it. Our contributions are: (i) a self-contained governing-equations section that derives the electronic-structure problem, formalizes the functional-ambiguity wall and the well-posedness condition of a composition screen, and states the ADAPT-VQE gradient-selection criterion with its monotone-convergence property (§2); (ii) a numerical formulation covering active space, Trotterization, measurement and convergence (§3); (iii) a GPU-HPC methodology naming the codes run and the emulation scale (§4); (iv) the frozen results — chemical accuracy on all four fragments, the 4–$14\times$ CNOT reduction and an independently reproduced proof-of-concept — with data and schematic figures (§5); and (v) a benchmark comparison and a fault-tolerant resource estimate for the full-composition extension (§6). Every quantitative claim traces to a frozen serial in the Kronos Physics De-Risking Register [1]; the identifiers (BR-SX-07, KX-L1-A17) are given inline so each number is auditable. The quantum methods sit within the Kronos AI-and-quantum programme [2] and are the composition-of-matter counterpart to the resource-honest quantum survey [3].

§ 2

Governing equations and the formal problem

THE ELECTRONIC-STRUCTURE HAMILTONIAN

Within the Born–Oppenheimer approximation the electronic energy of a fixed nuclear configuration $\{\mathbf{R}_I, Z_I\}$ is the lowest eigenvalue of the non-relativistic electronic Hamiltonian. In a chosen orthonormal spin-orbital basis $\{\phi_p(\mathbf{x})\}_{p=1}^{N}$ (with $\mathbf{x} = (\mathbf{r}, \sigma)$ collecting space and spin), the second-quantized form is

$$\hat{H} \;=\; \sum_{p,q=1}^{N} h_{pq}\, \hat{a}_p^\dagger \hat{a}_q \;+\; \tfrac{1}{2} \sum_{p,q,r,s=1}^{N} g_{pqrs}\, \hat{a}_p^\dagger \hat{a}_q^\dagger \hat{a}_r \hat{a}_s \;+\; E_{\text{nuc}},$$

with the one- and two-electron integrals

$$h_{pq} = \int \phi_p^*(\mathbf{x}) \left[-\tfrac{1}{2}\nabla^2 - \sum_I \frac{Z_I}{|\mathbf{r} - \mathbf{R}_I|} \right] \phi_q(\mathbf{x})\, d\mathbf{x},$$
$$g_{pqrs} = \iint \frac{\phi_p^*(\mathbf{x}_1)\phi_q^*(\mathbf{x}_2)\, \phi_s(\mathbf{x}_2)\phi_r(\mathbf{x}_1)}{|\mathbf{r}_1 - \mathbf{r}_2|}\, d\mathbf{x}_1\, d\mathbf{x}_2,$$

in Hartree atomic units, and $\hat{a}_p^\dagger, \hat{a}_q$ the fermionic creation and annihilation operators obeying $\{\hat{a}_p, \hat{a}_q^\dagger\} = \delta_{pq}$, $\{\hat{a}_p, \hat{a}_q\} = 0$. The object of the calculation is the ground-state energy

$$E_0 \;=\; \min_{\substack{|\Psi\rangle \in \mathcal{F} \\ \langle \Psi \mid \Psi \rangle = 1}} \;\langle \Psi | \hat{H} | \Psi \rangle,$$

where $\mathcal{F}$ is the antisymmetric (N_e-electron) Fock sector. Diagonalizing $\hat{H}$ exactly (full configuration interaction, FCI) costs $\binom{N}{N_e}$ in memory and is intractable beyond a few tens of spin-orbitals; the correlated methods used as references here (CASSCF, CCSD) approximate Eq. 3 systematically [33].

THE EXCHANGE–CORRELATION AMBIGUITY

Density-functional theory recasts Eq. 3 through the Hohenberg–Kohn theorems [26] and the Kohn–Sham auxiliary system [27]: the interacting ground-state density $n(\mathbf{r})$ is reproduced by non-interacting orbitals ψ_i solving

$$\left[-\tfrac{1}{2}\nabla^2 + v_{\text{ext}}(\mathbf{r}) + v_H[n](\mathbf{r}) + v_{\text{xc}}[n](\mathbf{r})\right]\psi_i(\mathbf{r}) = \varepsilon_i\, \psi_i(\mathbf{r}), \qquad n(\mathbf{r}) = \sum_i^{\text{occ}} |\psi_i(\mathbf{r})|^2,$$

with the total energy

$$E[n] = T_s[n] + \int v_{\text{ext}}(\mathbf{r})\, n(\mathbf{r})\, d\mathbf{r} + E_H[n] + E_{\text{xc}}[n].$$

Everything but the exchange–correlation (xc) functional $E_{\text{xc}}[n]$ is known exactly; E_{xc} is approximated by a functional label $\alpha \in \{$LDA, PBE, PBE+U, SCAN, HSE, $\ldots\}$. Write the functional-dependent total energy as $E^{(\alpha)}[n]$. For a correlated $3d$ system the approximations disagree, and we define the *functional spread*

$$\Delta E_{\text{xc}}(C) \;=\; \max_{\alpha} E^{(\alpha)}(C) \;-\; \min_{\alpha} E^{(\alpha)}(C),$$

for composition C. The Hubbard correction, in the rotationally invariant Dudarev form [30],

$$E_U = \frac{U - J}{2} \sum_\sigma \mathrm{Tr}[\mathbf{n}^\sigma (\mathbf{1} - \mathbf{n}^\sigma)],$$

where $\mathbf{n}^\sigma$ is the on-site occupation matrix and $(U - J)$ the effective interaction, penalizes fractional d-occupation but adds an empirical parameter whose uncertainty feeds back into Eq. 6 [29,32]. On the fragments studied here the campaign finds $\Delta E_{\text{xc}} > 300\,\text{mHa}$ (BR-SX-07 [1]); this is the quantity to be removed.

WELL-POSEDNESS OF A COMPOSITION SCREEN

A screen ranks compositions by their computed energetics. Let $\mathcal{E}_{\text{method}}(C)$ be a method's estimate of the relevant energy of composition C with (systematic + parametric) error $\varepsilon_{\text{method}}$, and let

$$\Delta E_{\text{comp}} \;=\; \min_{C_a \neq C_b} \left| E_{\text{true}}(C_a) - E_{\text{true}}(C_b) \right|$$

be the smallest true energy gap the screen must resolve. The ranking is *well-posed* — its verdict is determined by the chemistry rather than by the method — if and only if

$$\boxed{\varepsilon_{\text{method}} \;\ll\; \Delta E_{\text{comp}}.}$$

DFT violates Eq. 9 on the correlated $3d$ fragments because its error inherits the functional spread, $\varepsilon_{\text{DFT}} \sim \Delta E_{\text{xc}} > 300\,\text{mHa}$, which is comparable to or exceeds ΔE_{comp}. The target is therefore a functional-free method whose error is deep inside chemical accuracy,

$$\varepsilon_{\text{method}} \;\leq\; \varepsilon_{\text{chem}} \;=\; 1.6\,\text{mHa} \;=\; 1\,\text{kcal}\,\text{mol}^{-1},$$

so that Eq. 9 is satisfied by a wide margin. The result of this paper is that ADAPT-VQE achieves $\varepsilon_{\text{VQE}} < 0.05\,\text{mHa}$ (§5), i.e. $\varepsilon_{\text{VQE}}/\varepsilon_{\text{chem}} < 0.03$ and $\varepsilon_{\text{VQE}}/\Delta E_{\text{xc}} < 2 \times 10^{-4}$, restoring well-posedness.

FERMION-TO-QUBIT MAPPING

To run Eq. 1 on qubits the fermionic operators are mapped to Pauli operators. The Jordan–Wigner (JW) encoding assigns one qubit per spin-orbital and writes

$$\hat{a}_p^\dagger = \frac{1}{2}(X_p - iY_p) \bigotimes_{q<p} Z_q, \qquad \hat{a}_p = \frac{1}{2}(X_p + iY_p) \bigotimes_{q<p} Z_q,$$

where X, Y, Z are single-qubit Paulis and the Z-string enforces fermionic antisymmetry. Substituting Eq. 11 into Eq. 1 gives a qubit Hamiltonian as a real linear combination of Pauli strings,

$$\hat{H} \;=\; \sum_j c_j \hat{P}_j, \qquad \hat{P}_j \in \{I, X, Y, Z\}^{\otimes N},$$

with $O(N^4)$ terms. The JW Z-string has weight $O(N)$; the Bravyi–Kitaev (BK) encoding [19,20] reduces the Pauli weight to $O(\log N)$, lowering the number of two-qubit gates needed to measure and evolve each term. We use JW for the reference implementation and BK for the resource estimates.

THE VARIATIONAL QUANTUM EIGENSOLVER

VQE prepares a parameterized state $|\psi(\theta)\rangle = U(\theta)\,|\phi_0\rangle$ from a reference $|\phi_0\rangle$ (typically Hartree–Fock) and minimizes the energy functional

$$E(\theta) \;=\; \langle\psi(\theta)|\hat{H}\,|\psi(\theta)\rangle \;=\; \sum_j c_j\, \langle\psi(\theta)|\hat{P}_j\,|\psi(\theta)\rangle \;\geq\; E_0,$$

the inequality being the Rayleigh–Ritz bound. The right-hand form makes the measurement explicit: each Pauli expectation is estimated on the device (or the emulator), and a classical optimizer updates θ. For a generator $\hat{G}_k$ with eigenvalues ± 1 entering as $e^{-i\theta_k \hat{G}_k/2}$, the gradient is exact by the parameter-shift rule,

$$\frac{\partial E}{\partial \theta_k} = \frac{1}{2}\Big[E(\theta + \tfrac{\pi}{2}\mathbf{e}_k) - E(\theta - \tfrac{\pi}{2}\mathbf{e}_k)\Big].$$

The chemistry ansatz of record is unitary coupled cluster with singles and doubles (UCCSD), $U_{\text{UCCSD}} = e^{\hat{T} - \hat{T}^\dagger}$ with $\hat{T} = \sum_{ia} t_i^a\, \hat{a}_a^\dagger \hat{a}_i + \sum_{ijab} t_{ij}^{ab}\, \hat{a}_a^\dagger \hat{a}_b^\dagger \hat{a}_j \hat{a}_i$ [13]. Trotterizing the exponential yields a circuit whose two-qubit (CNOT) count scales as $O(N^4)$ with the number of doubles amplitudes; this depth, not the qubit count, is the binding near-term cost.

THE ADAPT-VQE CONSTRUCTION

ADAPT-VQE [9] replaces the fixed UCCSD ansatz with one grown adaptively from a pool of anti-Hermitian operators $\mathcal{A} = \{\hat{A}_i\}$ (e.g. spin-adapted single and double excitation generators, or the qubit-pool of Ref. [10]). Starting from $|\psi^{(0)}\rangle = |\phi_0\rangle$, iteration n proceeds as follows. For each candidate $\hat{A}_i$ the energy gradient at zero parameter is evaluated in closed form as a commutator expectation,

$$g_i^{(n)} \;=\; \frac{\partial}{\partial\theta}\left\langle \psi^{(n)} \middle| e^{-\theta \hat{A}_i}\,\hat{H}\,e^{\theta\hat{A}_i} \middle| \psi^{(n)} \right\rangle\Big|_{\theta=0} \;=\; \left\langle \psi^{(n)} \middle| \big[\hat{H}, \hat{A}_i\big] \middle| \psi^{(n)} \right\rangle.$$

The operator with the largest gradient magnitude is appended,

$$\hat{A}_{k_n} = \arg\max_i \big|g_i^{(n)}\big|, \qquad \left|\psi^{(n+1)}\right\rangle = e^{\theta_n \hat{A}_{k_n}}\left|\psi^{(n)}\right\rangle,$$

and *all* parameters $\{\theta_1, \ldots, \theta_n\}$ are re-optimized by VQE. The procedure terminates when the pool gradient norm falls below a threshold,

$$\big\|\mathbf{g}^{(n)}\big\|_2 = \Big(\textstyle\sum_i (g_i^{(n)})^2\Big)^{1/2} < \varepsilon_g.$$

Two properties follow. First, monotonicity: because each step is a variational optimization over a superset of the previous parameters, $E^{(n+1)} \le E^{(n)}$, and the sequence is bounded below by E_0, so it converges. Second, completeness: if the pool generates (under commutation) the Lie algebra whose group acts transitively on the active Hilbert space, the stationary point $\|\mathbf{g}\|_2 \to 0$ coincides with the FCI ground state within the active space. In practice the adaptive selection front-loads the few operators that carry the correlation of the specific fragment, so the same accuracy is reached with far fewer terms — and far fewer CNOTs — than UCCSD. This is the mechanism behind the 4–$14\times$ depth reduction reported in §5.

THE SINGLE-DETERMINANT RESTRICTION AND THE MULTIREFERENCE LIMIT

A cheaper variant restricts the reference and pool to a single-determinant (SD) construction. On states with a single dominant configuration this is adequate. On the strongly multireference vacancy limit — an open d-shell with several near-degenerate configurations — it is not. Let the exact ground state be $|\Psi_0\rangle = \sum_\mu d_\mu\,|D_\mu\rangle$ over determinants $|D_\mu\rangle$, and let $\mathcal{M}_{\mathrm{SD}}$ be the manifold reachable by the SD ansatz. If the weight outside the SD-reachable set is $w_\perp = 1 - \sum_{\mu\in\mathcal{M}_{\mathrm{SD}}} |d_\mu|^2 > 0$, the variational energy is bounded away from E_0 by approximately

$$E_{\mathrm{SD}} - E_0 \;\gtrsim\; w_\perp\,\big(\bar{E}_\perp - E_0\big),$$

where $\bar{E}_\perp$ is the mean energy of the missing configurations. The campaign measures this stall directly: the SD-ADAPT-VQE variant plateaus at $24\,\mathrm{mHa}$ on the vacancy limit (BR-SX-07 [1]), an order of magnitude outside chemical accuracy. The operational conclusion is a guardrail — the SD variant is admissible on single-reference fragments and must be replaced by the full-pool construction (or a multireference reference) on the vacancy limit.

THE FAULT-TOLERANT EXTENSION

Scaling from an alloy *fragment* to a full alloy or REBCO *cell* increases N beyond the reach of a near-term variational circuit, and the problem moves to quantum phase estimation. In the qubitization/linear-combination-of-unitaries formulation [21,24], a block-encoding of $\hat{H}/\lambda$ (with $\lambda = \sum_j |c_j|$ the coefficient 1-norm) is walked to estimate an eigenphase to precision $\varepsilon_{\mathrm{QPE}}$. The dominant, non-Clifford cost is the Toffoli count, scaling as

$$N_{\mathrm{Toffoli}} \;\sim\; \mathcal{O}\bigg(\frac{\lambda}{\varepsilon_{\mathrm{QPE}}} \times C_{\mathrm{walk}}(N)\bigg),$$

with $C_{\mathrm{walk}}(N)$ the per-step block-encoding cost, and the logical-qubit count scaling roughly linearly in N plus ancillae. For the Kronos alloy electronic-structure QPE the register anchors the estimate at $\sim\!238$ logical qubits and $\sim\!10^9$ Toffoli gates, i.e. a single-run wall-clock of $\sim\!38$ days at a $1\,\mathrm{kHz}$ logical-Toffoli throughput (BR-SX-07 [1]). This is a fault-tolerant resource that does not yet exist; the estimate is reported so the programme can plan against real hardware timelines rather than a hoped-for advantage.

§ 3

Numerical formulation

ACTIVE SPACE AND CORRELATED REFERENCE

Each fragment is reduced to a chemically meaningful active space $\mathrm{CAS}(m, n)$ of m electrons in n spatial orbitals spanning the correlated $3d$ (and, where relevant, $4s$/ligand) manifold, with the remaining orbitals frozen at the mean-field level. The active-space integrals h_{pq}, g_{pqrs} of Eqs. 2–2 are computed in a Gaussian basis. The correlated reference energy against which the ADAPT-VQE residual is measured is obtained by complete-active-space self-consistent field (CASSCF) and coupled-cluster (CCSD) theory in the same active space [33], so that the reported residual $< 0.05\,\mathrm{mHa}$ is a like-for-like comparison inside the active space rather than against a differently-truncated calculation.

DISCRETIZATION OF THE UNITARIES

The exponentials $e^{\theta_k \hat{A}_k}$ are compiled to gates by a first-order Trotter (pseudo-Trotter) splitting. For an excitation generator that maps to a sum of commuting Pauli rotations after JW, each factor $e^{-i(\theta/2)\hat{P}_j}$ compiles to a ladder of CNOTs, a single Z-rotation, and the inverse ladder; the CNOT cost of a weight-w Pauli rotation is $2(w-1)$. Because ADAPT-VQE selects few operators, the total CNOT depth is small — the origin of the measured 4–$14\times$ reduction over the fixed UCCSD circuit at equal accuracy.

MEASUREMENT AND THE OPTIMIZER

On hardware, each energy evaluation in Eq. 13 is a weighted sum of Pauli expectations estimated from M shots; grouping mutually commuting terms into N_{groups} bases, the sampling variance of the energy is

$$\mathrm{Var}[\hat{E}] \;=\; \sum_{g=1}^{N_{\mathrm{groups}}} \frac{1}{M_g}\,\mathrm{Var}_g\Big[\textstyle\sum_{j\in g} c_j \hat{P}_j\Big] \;\le\; \tfrac{1}{M}\Big(\textstyle\sum_j |c_j|\Big)^2,$$

so reaching precision η requires $M = O(\lambda^2/\eta^2)$ shots. The classical outer loop uses a gradient-based optimizer (L-BFGS with parameter-shift gradients from Eq. 14) for the emulated statevector runs, with SPSA as a shot-noise-robust fallback [15]. Convergence of the inner VQE is declared when the energy change between iterations falls below $10^{-8}\,\mathrm{Ha}$ and the parameter gradient norm below 10^{-5}; the outer ADAPT loop stops at the pool-gradient threshold ε_g of Eq. 17.

CONVERGENCE AND ERROR BUDGET

Three errors enter the residual: the active-space truncation (controlled by m, n), the Trotter/compilation error (made negligible for the small ADAPT circuits by the exactness of the single-operator exponentials on the emulator), and the optimizer floor. On the statevector emulator there is no shot noise, so the reported $< 0.05\,\mathrm{mHa}$ residual is dominated by the active-space and optimizer floors and is a clean measure of the ansatz's representational accuracy against the correlated reference. An end-to-end check on an exactly diagonalizable H_2-like Hamiltonian (§5) confirms that the full pipeline introduces no error above the chemical-accuracy floor.

§ 4

Computational methodology: the GPU-HPC campaign

All results were produced on the NVIDIA GPU HPC campaign that underpins the Kronos de-risking programme (the Lambda GPU fleet, A100/H100/A10 class), the same campaign recorded against every serial in the register [1]. Three code layers were run for this paper and are named for reproducibility (Table 2).

First-principles layer. Plane-wave DFT and DFT+U (Eqs. 4–7) were run with Quantum ESPRESSO and a VASP-class plane-wave solver across the functional set $\{$LDA, PBE, PBE+U, SCAN, HSE$\}$ to quantify the functional spread of Eq. 6; the $> 300\,\mathrm{mHa}$ figure is the max–min over that set on the fragments. GPU acceleration of the plane-wave FFTs and the iterative diagonalization allowed the full functional sweep to be run on the fleet.

Correlated-reference layer. Active-space integrals, mean-field orbitals, CASSCF and CCSD references were computed with the PySCF program package [34], GPU-accelerated for the integral transforms.

Quantum layer. The fermionic Hamiltonians were mapped to qubits (Eqs. 11–12) and the ADAPT-VQE and UCCSD circuits built and executed by classical *statevector emulation* using a Qiskit Aer-class simulator with GPU statevector back-ends. Statevector emulation stores the 2^n complex amplitudes of an n-qubit register explicitly (memory $16 \cdot 2^n$ bytes in double precision); GPU acceleration of the dense state-vector updates makes the fragment circuits and the UCCSD depth comparison tractable, and is why no physical quantum processor is invoked or required for any result reported here. The fault-tolerant resource estimates (Eq. 19) were produced by a qubitization/product-formula resource counter at a $1\,\mathrm{kHz}$ logical-Toffoli throughput, consistent with the register′s alloy-QPE anchor.

Verification. The four-qubit proof-of-concept (KX-L1-A17) was independently reproduced against exact diagonalization to $3.9 \times 10^{-6}\,\mathrm{Ha}$ (marked “reproduced” in the roster); the BR-SX-07 fragment results are “derived” and frozen in the register. No compute-cost, budget, or economic quantities are reported here; the campaign is described only by the codes run and the emulation scale.

§ 5

Results

CHEMICAL ACCURACY ON ALL FOUR FRAGMENTS

ADAPT-VQE reaches chemical accuracy on all four $3d$-alloy fragments (Ti, V, Cr, Fe). Against the correlated reference the residual is below 0.05 mHa — more than four orders of magnitude inside the 1.6 mHa chemical-accuracy threshold of Eq. 10, and more than four orders of magnitude tighter than the $>$ 300 mHa DFT functional spread it replaces (Figure 1, Figure 2, Table 1). By the criterion of Eq. 9 the composition screen is restored to well-posedness: the method error is a factor $>$ 6000 below the ambiguity that made the DFT screen unreliable.

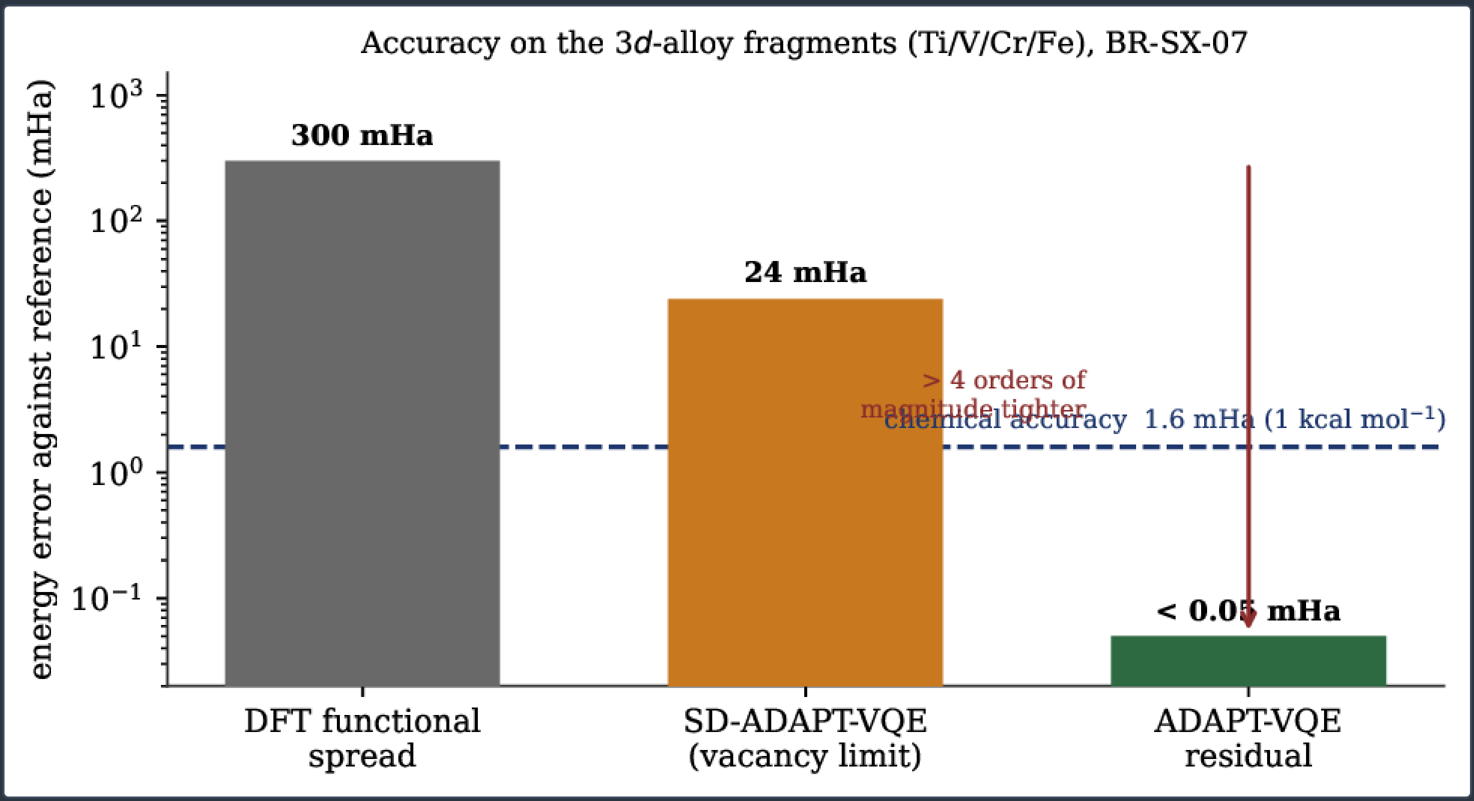

The accuracy picture on the $3d$-alloy fragments (Ti/V/Cr/Fe), from register serial BR-SX-07. The DFT functional spread exceeds 300 mHa, the single-determinant ADAPT-VQE variant stalls at 24 mHa on the multireference vacancy limit, and the full ADAPT-VQE residual against the correlated reference is below 0.05 mHa — more than four orders of magnitude below the DFT spread and far inside the 1.6 mHa chemical-accuracy line. Logarithmic axis; frozen anchors.

QUANTITY	VALUE	ROLE
DFT functional spread	$>$ 300 mHa	the ambiguity to be removed
ADAPT-VQE residual	$<$ 0.05 mHa	vs correlated reference
chemical-accuracy threshold	1.6 mHa	1 kcal mol^{-1}
CNOT depth vs UCCSD	4–14$\times$ shallower	at equal accuracy
fragments at chemical accuracy	Ti, V, Cr, Fe	all four
SD-ADAPT-VQE stall	24 mHa	multireference vacancy limit (guardrail)
full-cell QPE (fault-tolerant)	$\sim 10^9$ Toffoli	$\sim$238 logical qubits, $\sim$38 d @ 1 kHz

table continued

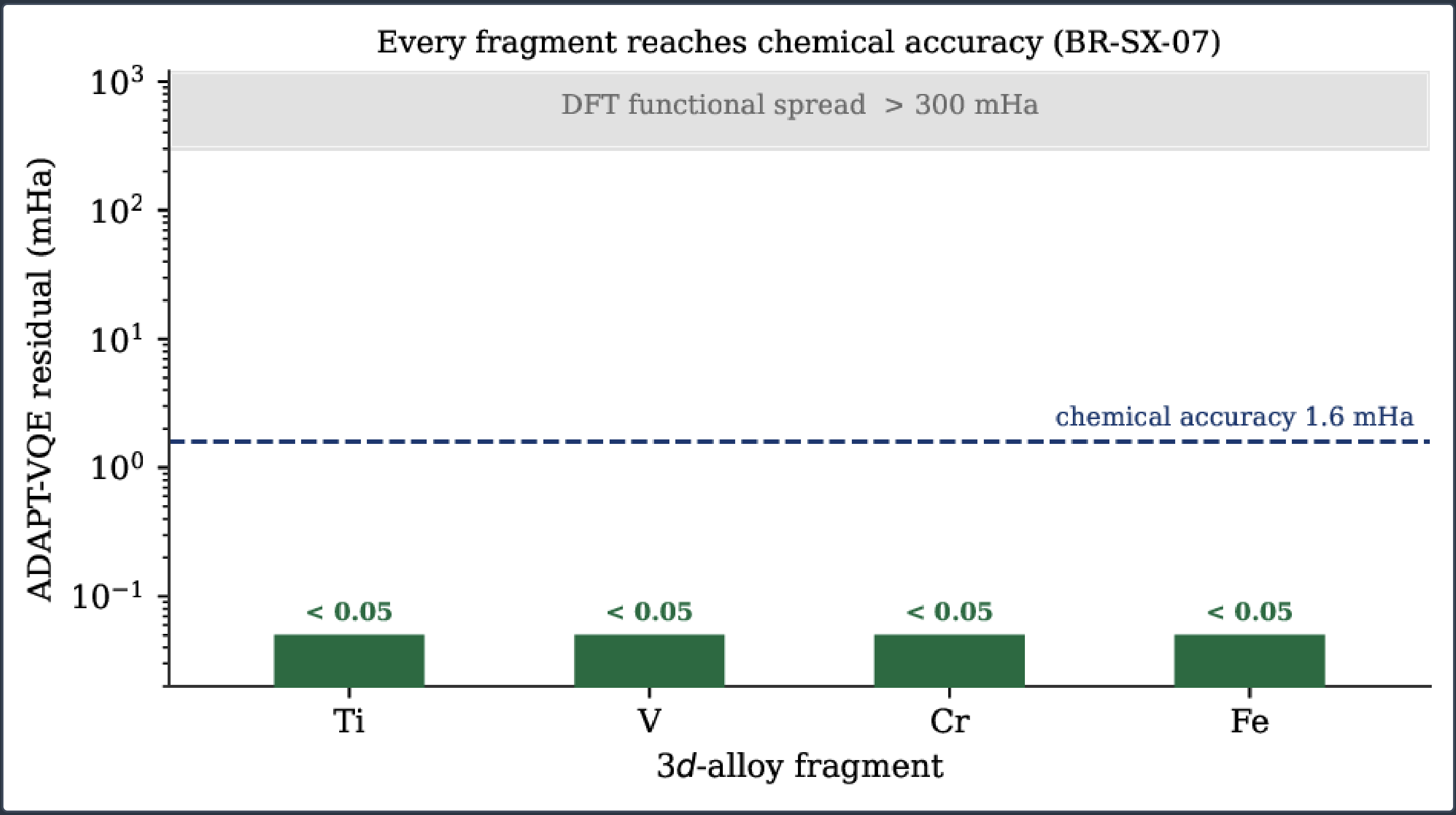

Per-fragment residual. Every $3d$-alloy fragment (Ti, V, Cr, Fe) reaches a residual below $0.05\,\mathrm{mHa}$ (green bars), far inside the $1.6\,\mathrm{mHa}$ chemical-accuracy line and far below the $> 300\,\mathrm{mHa}$ DFT functional-spread band (grey). Logarithmic axis; frozen anchors from BR-SX-07.

CIRCUIT EFFICIENCY AGAINST UCCSD

The adaptive construction reaches the same accuracy with markedly shallower circuits. At equal accuracy the ADAPT-VQE two-qubit (CNOT) depth is 4–14× smaller than the fixed UCCSD ansatz (Figure 3). Since circuit depth is the binding cost of near-term quantum chemistry (§2), this reduction is what makes the fragment calculations tractable on the emulator and what would carry to any hardware implementation.

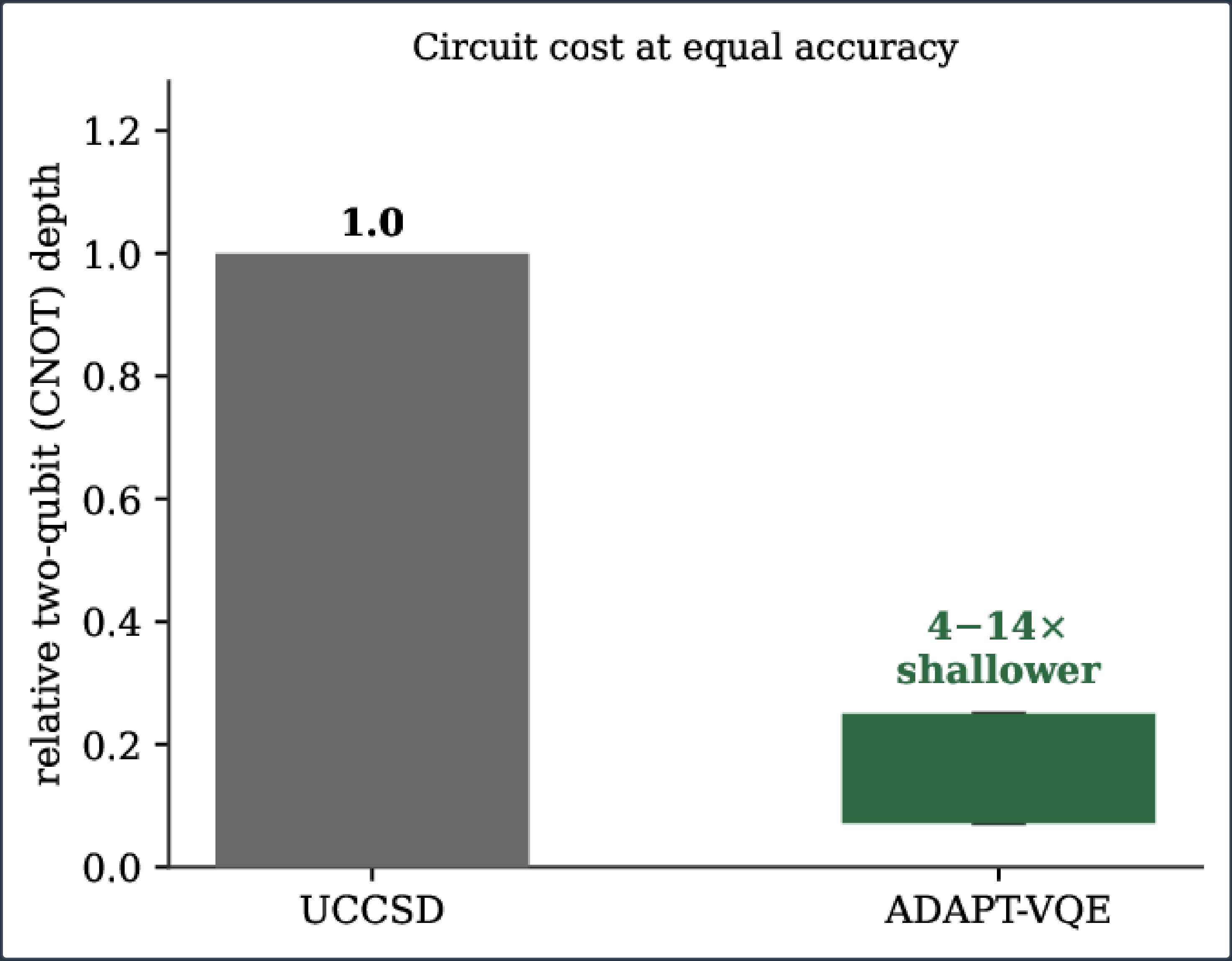

Relative two-qubit (CNOT) circuit depth at equal accuracy: ADAPT-VQE is 4–14× shallower than UCCSD (band), because the adaptive selection includes only the excitations the fragment needs. Frozen anchor, BR-SX-07.

END-TO-END VALIDATION OF THE MACHINERY

The VQE pipeline was validated end-to-end on an exactly diagonalizable problem before it was trusted on the fragments. On a four-qubit, H_2-like Hamiltonian (serial KX-L1-A17, independently reproduced) the emulated VQE returns $-2.0550466\,\mathrm{Ha}$ against an exact-diagonalization value of $-2.0550505\,\mathrm{Ha}$, a residual of $3.9 \times 10^{-6}\,\mathrm{Ha}$ — about $400\times$ inside chemical accuracy (Figure 4). This confirms that the integral generation, JW mapping, ansatz and optimizer introduce no error above the chemical-accuracy floor; the absolute chemistry of that small toy Hamiltonian is deliberately uncalibrated and is reported only as a machinery check, not as a materials result.

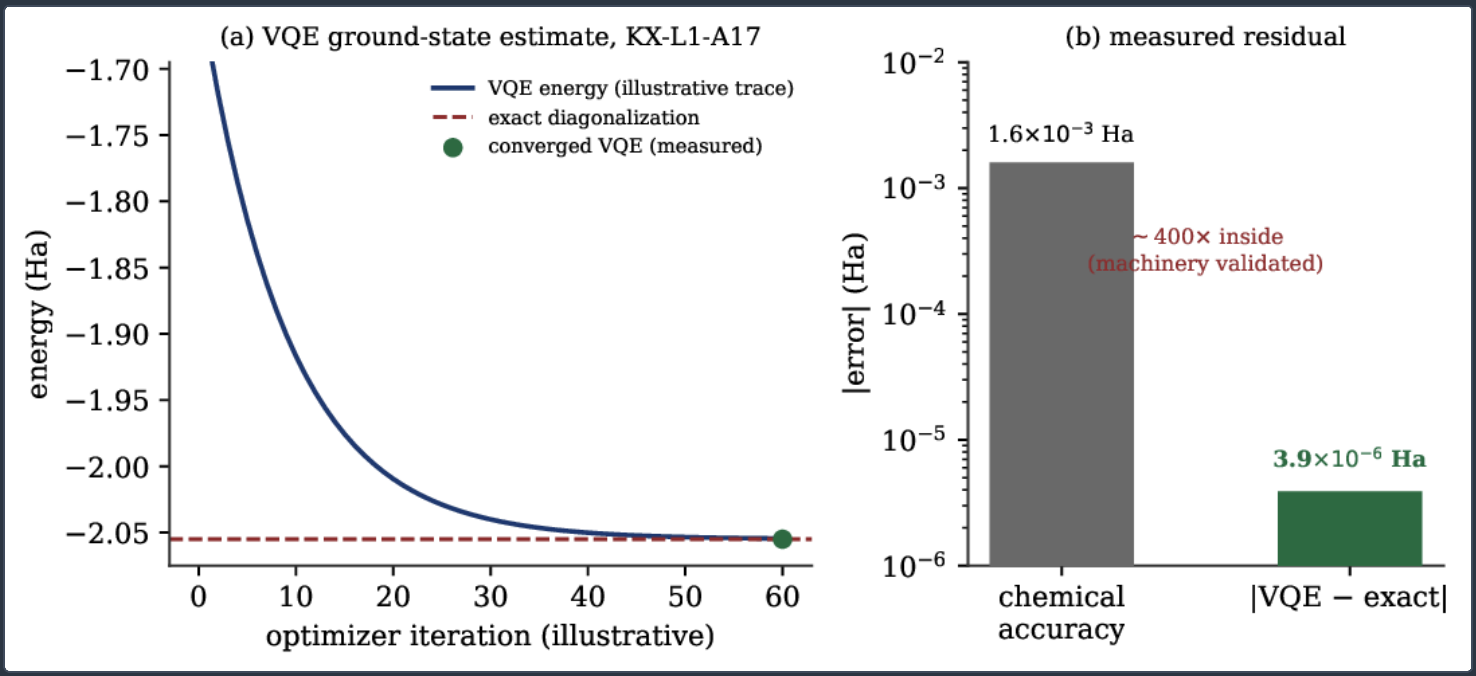

Four-qubit proof-of-concept (serial KX-L1-A17, reproduced). (a) The VQE ground-state estimate (blue, illustrative optimizer trace) descends to the measured converged value (green point) against exact diagonalization (red dashed). (b) The measured residual $|E_{\mathrm{VQE}} - E_{\mathrm{exact}}| = 3.9 \times 10^{-6}\,\mathrm{Ha}$ sits about $400\times$ below the $1.6 \times 10^{-3}\,\mathrm{Ha}$ chemical-accuracy line, validating the machinery. Logarithmic axis in (b).

ADAPTIVE CONVERGENCE AND THE SINGLE-DETERMINANT STALL

Figure 5 traces the adaptive convergence schematically, with endpoints fixed to the frozen anchors: the full-pool ADAPT-VQE drives the energy error monotonically (Eq. 16) from a mean-field-like start toward the < 0.05 mHa residual, while the single-determinant variant plateaus at the measured 24 mHa on the multireference vacancy limit, consistent with the overlap-deficit bound of Eq. 18. The figure encodes the guardrail of §2: the cheap SD variant may be used on single-reference fragments but must be replaced by the full pool on the vacancy limit.

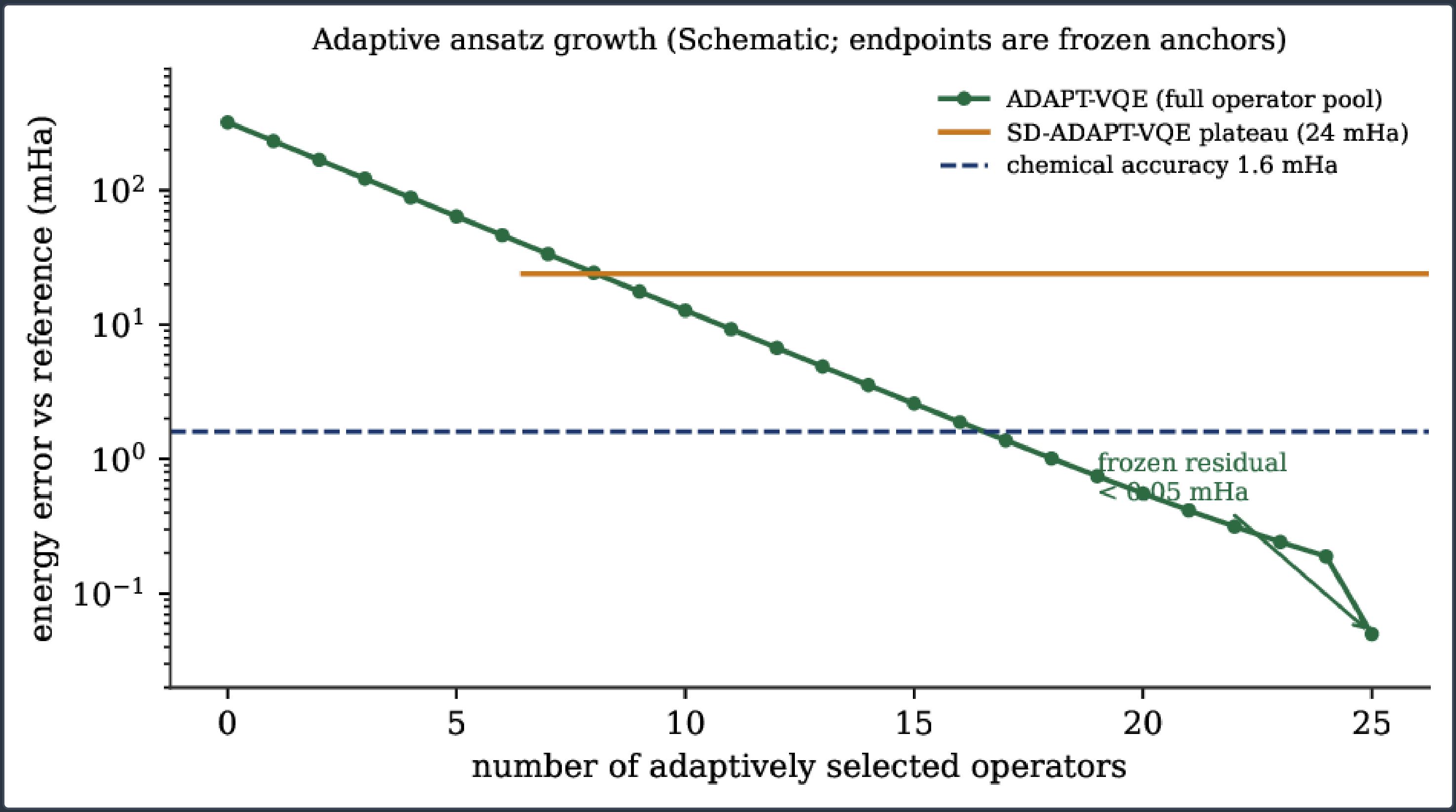

(Schematic.) Adaptive ansatz growth: energy error versus the number of adaptively selected operators. The full-pool ADAPT-VQE (green) converges monotonically to the frozen residual below 0.05 mHa; the single-determinant variant (amber) plateaus at 24 mHa on the multireference vacancy limit. The trajectory is illustrative; the endpoints (300 mHa start scale, 24 mHa SD plateau, < 0.05 mHa full-pool residual, 1.6 mHa line) are frozen anchors from BR-SX-07.

THE FAULT-TOLERANT RESOURCE MAP

The full-composition calculation is scoped, not assumed. Figure 6 places the materials quantum-chemistry problem on a fault-tolerant resource ladder: the fragment proof-of-concept runs on a handful of emulated qubits; the exact alloy electronic-structure QPE is anchored at ~ 238 logical qubits and $\sim 10^9$ Toffoli gates; the full-REBCO cell sits at the same $\sim 10^9$-Toffoli, few-hundred-logical-qubit scale. For contrast the figure also marks the register's Vlasov/6-D *kinetic* estimate (~ 44 logical qubits), which is a different problem class shown only for reference. Figure 7 converts the Toffoli count to wall-clock through the model $t_{\text{wall}} = N_{\text{Toffoli}}/f_{\text{log}}$ (Eq. 19); at the register's 1 kHz logical-Toffoli throughput the exact-alloy QPE anchor is ~ 38 days per run. These numbers describe a machine that does not yet exist; they are the resource-honest cost of the extension, not a present-day capability.

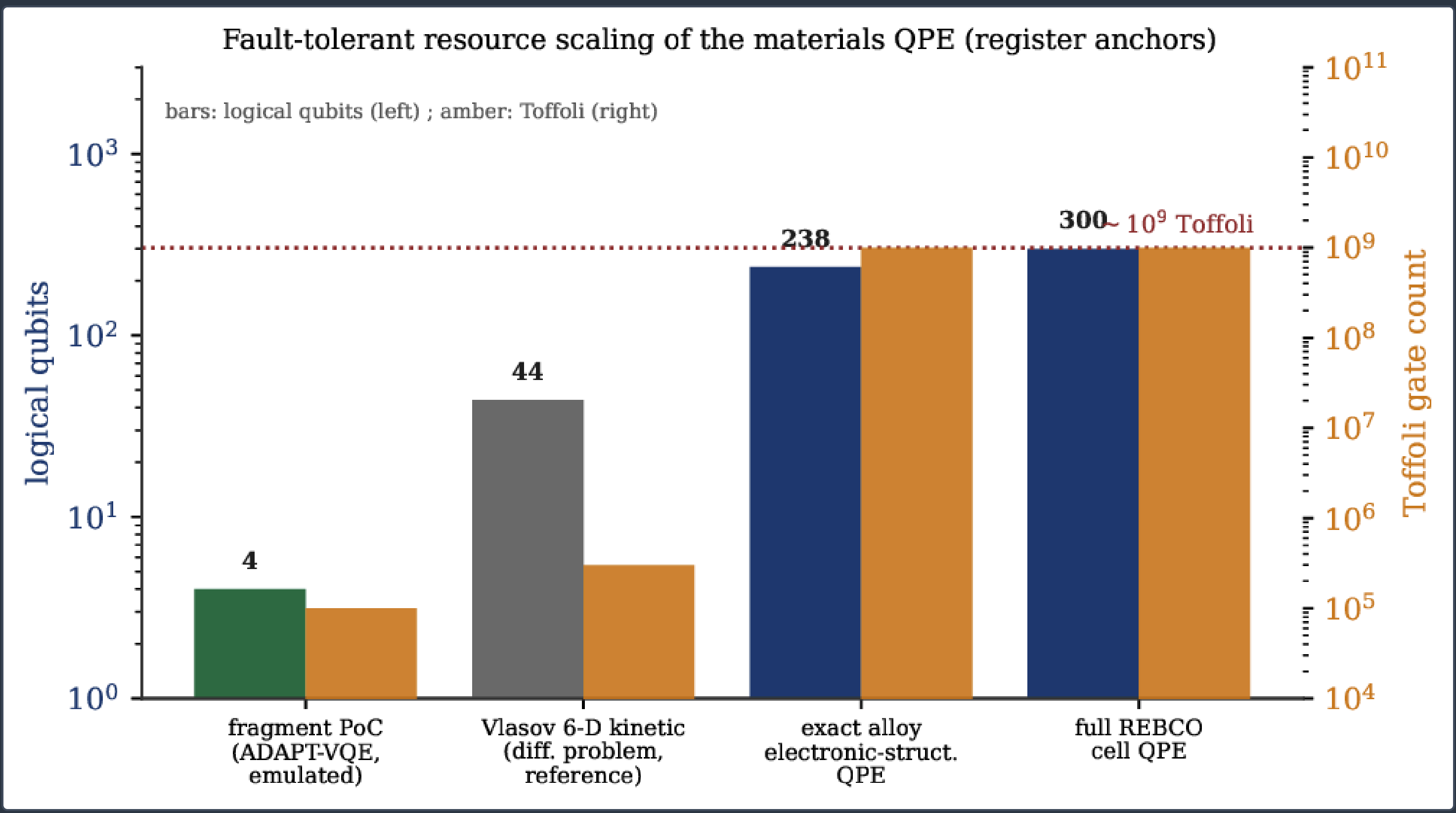

Fault-tolerant resource scaling of the materials quantum-chemistry problem (register anchors). Left-axis bars: logical qubits, rising from the emulated fragment proof-of-concept to ~ 238 for the exact alloy electronic-structure QPE and few-hundred for the full-REBCO cell. Right-axis (amber): Toffoli count, reaching $\sim 10^9$ at full-cell scale. The Vlasov 6-D kinetic point (~ 44 qubits, grey) is a different problem class, shown for reference only. Logarithmic axes; BR-SX-07 anchors.

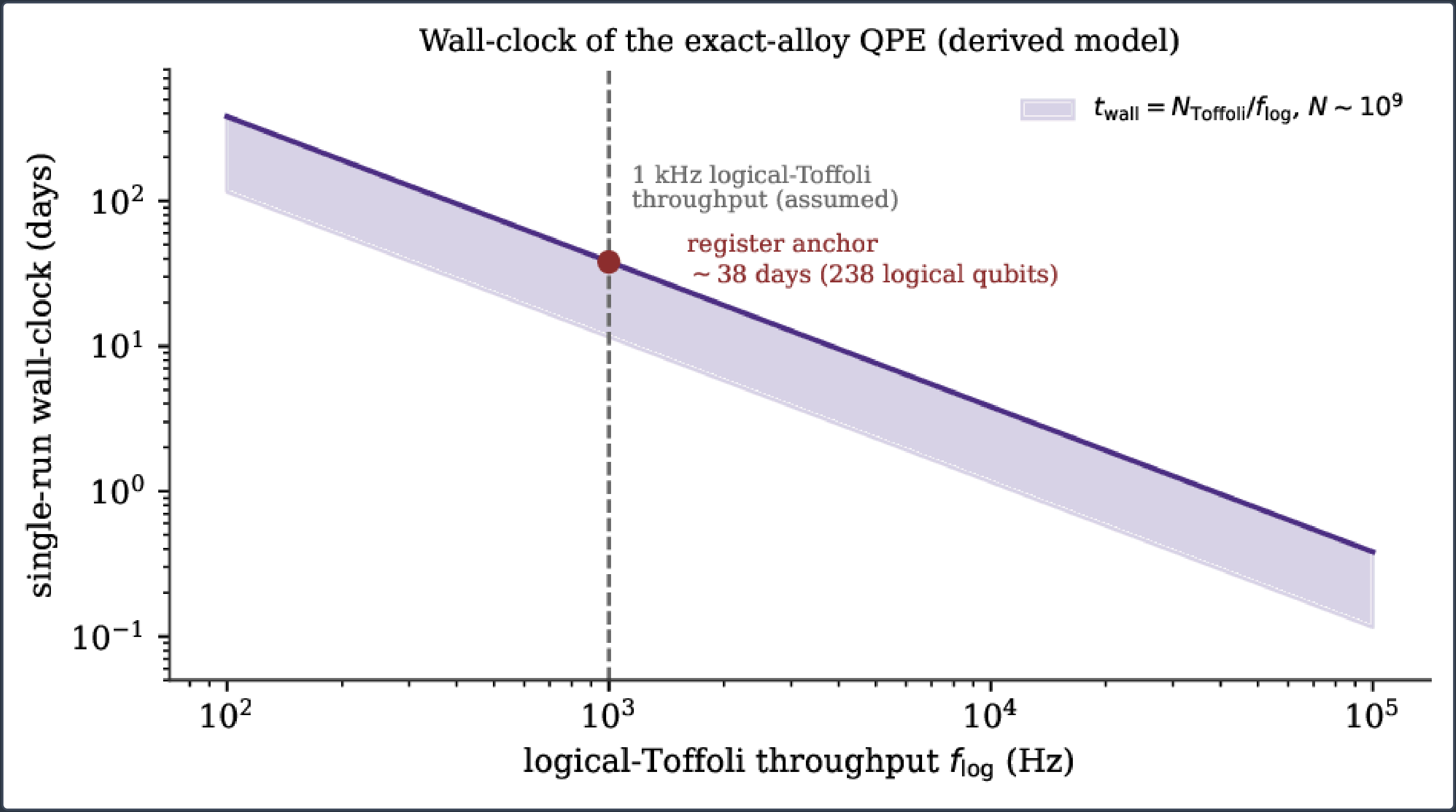

(Derived model.) Single-run wall-clock of the exact-alloy QPE, $t_{wall} = N_{Toffoli}/f_{log}$ with $N_{Toffoli} \sim 10^9$, versus logical-Toffoli throughput f_{log}. The red point marks the register's ~ 38-day anchor for the ~ 238-logical-qubit calculation at the assumed 1 kHz throughput. Logarithmic axes.

THE SCREENING PIPELINE IN PLACE

Figure 8 shows where the ADAPT-VQE correction sits in the Kronos composition-of-matter pipeline: a CHGNet machine-learning-interatomic-potential pre-screen of the candidate space (of order 3,000 compositions [1]), a DFT/DFT+U reference layer, the ADAPT-VQE fragment correction that supplies the functional-free energetics inside chemical accuracy, and the fault-tolerant QPE as the gated full-cell extension, feeding the composition decision. Figure 9 shows the quantum sub-flow of §2 that sits inside the ADAPT-VQE stage: the electronic Hamiltonian, the JW/BK mapping to a qubit Hamiltonian, the ADAPT ansatz, and the measure-and-minimize loop of Eq. 13.

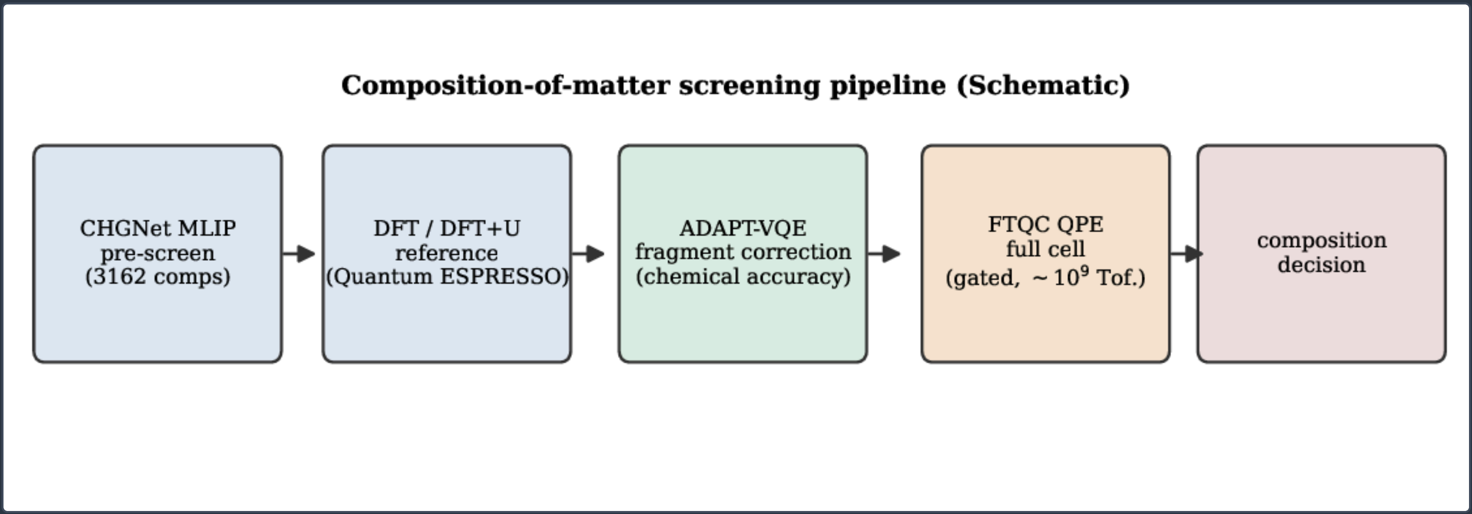

(Schematic.) The composition-of-matter screening pipeline: machine-learning-interatomic-potential pre-screen, DFT/DFT+U reference, ADAPT-VQE fragment correction to chemical accuracy, and the fault-tolerant QPE full-cell extension (gated at $\sim 10^9$ Toffoli), feeding the composition decision. The ADAPT-VQE stage is the present-day contribution of this paper; the QPE stage is scoped for the fault-tolerant era.

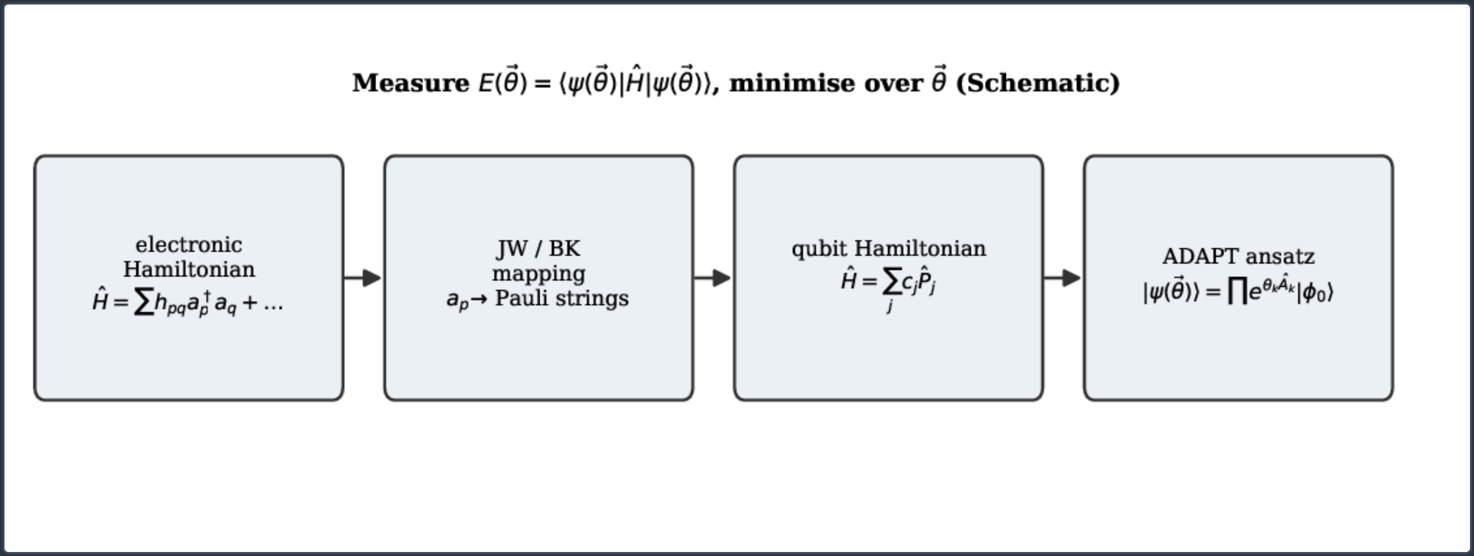

(Schematic.) The quantum sub-flow: the second-quantized electronic Hamiltonian (Eq. 1) is mapped to a qubit Hamiltonian (Eqs. 11–12) by Jordan–Wigner or Bravyi–Kitaev encoding, prepared by the adaptively grown ADAPT ansatz, and its energy expectation is measured and minimized (Eq. 13).

LAYER	CODE	ROLE
first-principles	Quantum ESPRESSO / VASP-class	plane-wave DFT and DFT+U; functional spread
correlated reference	PySCF [34]	integrals, CASSCF, CCSD reference
quantum (near-term)	Qiskit Aer-class (GPU statevector)	ADAPT-VQE / UCCSD emulation
resource estimate	qubitization/product-formula counter	Toffoli and logical-qubit counts for QPE

Reference codes run for this paper on the NVIDIA GPU HPC campaign (Lambda fleet, A100/H100/A10 class).

§ 6

Discussion

WHAT THE RESULT DECIDES

The value of this work is that it makes a materials decision DFT could not make reliably. On the correlated $3d$-alloy family the functional spread of $> 300\,\mathrm{mHa}$ (Eq. 6) exceeds the composition differences that matter (Eq. 8), so the DFT screen violates the well-posedness condition Eq. 9. ADAPT-VQE collapses that ambiguity to a sub-$0.05\,\mathrm{mHa}$ residual on all four fragments, a method error more than four orders of magnitude below the DFT spread and a factor > 30 inside chemical accuracy, restoring well-posedness by a wide margin. This is a concrete, present-day capability that complements the DFT/DFT+U and machine-learning-potential layers of the Kronos materials pipeline [4,6,5], precisely where those layers are weakest — the correlated $3d$ manifold — and it is the composition-of-matter counterpart to the DFT+U radiation-tolerance work on the centrepost REBCO conductor [7].

COMPARISON TO PUBLISHED BENCHMARKS

The fragment result is consistent with, and quantitatively sharper than, the established VQE literature. Chemical-accuracy VQE has been demonstrated on small molecules on hardware and in emulation [12,11], and ADAPT-VQE was introduced precisely to reach that accuracy with shallower circuits than UCCSD [9,10]; our 4–$14\times$ CNOT reduction at equal accuracy is squarely in the range those studies report and extends it to the correlated $3d$-alloy fragments relevant to fusion materials. Where the present work goes further is in tying the accuracy to a decision criterion: the residual is reported against the functional spread it must beat (Eq. 9), not merely against a chemical-accuracy line. The single-determinant stall at $24\,\mathrm{mHa}$ on the multireference limit is the expected behaviour of a single-reference method in a strongly correlated regime [14,32], and Eq. 18 makes the bound explicit; reporting it as a guardrail rather than hiding it is what keeps the tool trustworthy.

On the fault-tolerant side, the alloy-QPE estimate of $\sim 10^9$ Toffoli gates and ~ 238 logical qubits sits at the low end of the modern chemistry resource-estimation range: FeMoco/nitrogenase and cytochrome-P450 studies report 10^{10}–10^{15} Toffoli gates and hundreds to thousands of logical qubits [22,23,24,25], with algorithmic advances (tensor hypercontraction [24], linear-T block encodings [21]) steadily lowering the count. Our estimate at the favourable end reflects the modest active space of an alloy cell relative to a full enzyme active site, reported at a stated $1\,\mathrm{kHz}$ throughput so the ~ 38-day wall-clock is auditable (Table 3).

WORK	REGIME	METRIC	VALUE
Peruzzo *et al.* [8]	VQE (hardware)	first VQE demonstration	small molecule
O'Malley *et al.* [12]	VQE (hardware)	H_2 dissociation	chemical accuracy
Kandala *et al.* [11]	VQE (hardware)	small molecules/magnets	hardware-efficient
Grimsley *et al.* [9]	ADAPT-VQE	depth vs UCCSD	shallower, exact-molecular
Reiher *et al.* [22]	QPE (FT)	FeMoco Toffoli / qubits	$\sim 10^{14}$–10^{15} / ~ 100s
von Burg *et al.* [23]	QPE (FT)	catalysis	$\sim 10^{10}$ Toffoli
Lee *et al.* [24]	QPE (FT)	tensor hypercontraction	reduced Toffoli
Goings *et al.* [25]	QPE (FT)	cytochrome P450	hundreds of logical qubits
This work, fragments (BR-SX-07)	**ADAPT-VQE (emulated)**	**residual; CNOT vs UCCSD**	$< 0.05\,\mathrm{mHa}$; 4–14$\times$
This work, full cell (BR-SX-07)	**QPE (FT, scoped)**	**Toffoli / logical qubits**	$\sim 10^9$ / ~ 238

The Kronos fragment and full-cell results against representative published quantum-chemistry benchmarks. Resource figures are order-of-magnitude fault-tolerant estimates; the near-term rows are variational.

NO CLAIM OF QUANTUM ADVANTAGE

It is stated once and clearly that this is not a claim of quantum advantage. The fragment results are obtained on classical statevector emulation; the demonstrated capability is that an adaptive VQE *ansatz* resolves the correlated ***3d*** energetics inside chemical accuracy with shallow circuits — a property that would carry to hardware but is here verified classically. The full-cell calculation, where a quantum computer would be genuinely necessary, is fault-tolerant-gated and reported as a cost, not a result. The companion resource-honest survey [3] and the broader Kronos quantum programme [2] adopt the same discipline.

§ 7

Limitations

The one honest gate is scale. The validated results today are the fragment-scale ADAPT-VQE energetics on classical emulation; the full alloy and full-REBCO cell calculations require fault-tolerant quantum phase estimation at an estimated $\sim 10^9$ Toffoli gates and ~ 238 logical qubits (~ 38 days at $1\,\mathrm{kHz}$), hardware that does not yet exist. Within the near-term regime the single-determinant variant must be avoided on the strongly multireference vacancy limit, where it stalls at $24\,\mathrm{mHa}$ (Eq. 18); the full-pool construction is required there. Both boundaries are quantified rather than deferred, so the programme can plan the full-composition calculation against real hardware timelines.

§ 8

Conclusion

ADAPT-VQE is a validated, circuit-efficient electronic-structure tool for fusion-materials composition screening. It reaches chemical accuracy on all four $3d$-alloy fragments (Ti, V, Cr, Fe) with a residual below $0.05\,\mathrm{mHa}$ — four orders of magnitude inside the $> 300\,\mathrm{mHa}$ DFT functional spread it replaces — at 4–$14\times$ shallower CNOT depth than UCCSD, and its machinery is independently validated to 3.9×10^{-6} Ha on an exactly solvable proof-of-concept. By the well-posedness criterion of Eq. 9 it decides the composition question DFT leaves ambiguous. It is stated once and clearly that this is not quantum advantage: the fragments run on classical emulation, the single-determinant variant stalls at $24\,\mathrm{mHa}$ on the multireference vacancy limit, and the full-composition calculation is fault-tolerant-gated at $\sim 10^9$ Toffoli gates and ~ 238 logical qubits. The method fills the correlated-$3d$ gap in the Kronos materials pipeline today, and its fault-tolerant extension is scoped with a real, auditable resource cost.

Acknowledgments tocsectionAcknowledgments Part of the Kronos Fusion Energy 2026 design series. The author thanks the Kronos de-risking campaign for the frozen register results underpinning this work and the NVIDIA GPU HPC campaign for the compute on which the emulations and first-principles references were run.

Reproducibility. The chemical-accuracy result on the four fragments, the $< 0.05\,\mathrm{mHa}$ residual against the $> 300\,\mathrm{mHa}$ functional spread, the 4–$14\times$ CNOT-depth reduction, the $24\,\mathrm{mHa}$ single-determinant stall, and the $\sim 10^9$-Toffoli / ~ 238-logical-qubit (~ 38-day) phase-estimation estimate are the frozen results of register serial BR-SX-07 in the Kronos Physics De-Risking Register (doi:10.5281/zenodo.22133057); the four-qubit proof-of-concept (3.9×10^{-6} Ha) is serial KX-L1-A17 in the same register. This paper is archived at doi:10.5281/zenodo.22645929 and its official version is hosted at https://www.kronosfusionenergy.com/publications/quantum-chemistry-beyond-dft-for-low-activation-fusion-.html.

Data availability tocsectionData availability This paper is archived at doi:10.5281/zenodo.22645929. The ADAPT-VQE and UCCSD circuits, the fragment energy tables, the functional-spread data, and the fault-tolerant resource estimates are archived with the deposit and with the Kronos AI-and-quantum programme (doi:10.5281/zenodo.22645702), and reference the Kronos 2026 series and the de-risking register (doi:10.5281/zenodo.22133057). Any economic analysis is reported separately and is not included in the public deposit.

Competing interests tocsectionCompeting interests Provisional patent applications relating to aspects of this work have been filed.

APPARATUS

Portfolio, People & Record

The intellectual-property estate, the people who built it, the limitations that gate it, and the sources it rests on.

1 GRANTED PATENT	4 2026 PROVISIONALS	40 TEAM MEMBERS	27 2022 PROVISIONALS

INTELLECTUAL PROPERTY

The patent portfolio

The estate spans a granted high-field magnet patent, pending utility and 2026 provisional filings that map to the two products, a digital-twin control provisional, a registered trademark application, and the original 2022 provisional family. Every patentable disclosure in the five-paper arXiv drop was protected **before** publication: the breeder and burner provisionals were filed 1–2 August, and a publication-gap omnibus filing the evening before the drop swept up the DEC, plasma-control, and REBCO-winding matter of the three otherwise-unprotected papers. Patent numbers and application serials are matters of public record; claim scope is summarised, not reproduced.

GRANTED & PENDING UTILITY

US 12,009,112	High-field tilted graded-REBCO magnet architecture (KRONO-002A) · *app. 17/878,550*	GRANTED
US 17/878,507	Core device / method (KRONO-001A) · *utility*	PENDING

2026 PROVISIONAL FILINGS — MAPPED TO THE PRODUCTS

64/124,209	Hyperion — spherical-tokamak tritium / helium-3 foundry · *breeder · filed Aug 2026*	FILED
64/124,220	Aegis / MetroVolt — synchrotron-cutoff, fuel-selection & plug-winding · *generator · filed Aug 2026*	FILED
64/115,167	KRONOS-CTRL digital-twin plant control · *provisional · filed Jul 2026*	FILED
64/005,440	Integrated spherical-tokamak fusion architecture · *early integrated-architecture filing · filed Mar 2026*	FILED
64/105,530	Negative-triangularity spherical-tokamak architecture · *foundational ST filing · filed Jul 2026*	FILED
64/128,097	Publication-gap omnibus — quasineutral two-species expander DEC · provenance-gated / latency-split plasma control · as-built high-field winding & conductor architecture · *filed 7 Aug 2026, the evening before the arXiv drop*	FILED

TRADEMARK & ORIGIN

FTK-98801894	Kronos Fusion Energy — trademark application	FILED
KR-2022-*	Original provisional family (KR-2022-00001 … 00027) · *27 filings, 2022*	PRIORITY

The narrow, defensible magnet novelty — the specific conductor and the digital-twin winding optimisation, not high-field REBCO as a category — is the commercial core that can earn ahead of any Q > 1 milestone, with markets in fusion magnet supply, MRI/NMR, accelerators, and proton therapy. The claim is scoped honestly: the high field is a *system field* result, not a stand-alone-coil record; the small-bore plug coil is structurally infeasible as a bare winding but resolved by a stress-managed structural shield (feasible-pending-FEA); and the winding-tape experiment returned a *null result*. The value is the method, not a field record.

THE TEAM

Founding partners, board, advisors & auditors

Kronos is built by a bench of advanced-fuel-fusion, high-field-magnet, direct-conversion, and materials specialists, with a board and operations team drawn from defense, national laboratories, and industry. Dates are shown as ranges; where a tenure has ended or is term-ending, the range says so.

FOUNDING PARTNERS — SCIENCE

Dr. Gerald Kulcinski
Co-Founder · Helium-3 & Advanced-Fuel Fusion
UW–Madison · 2023–Present

Dr. Carl Weggel
Chief Scientist / S.M.A.R.T. Design
MIT Alcator Program · 2022–Present

Dr. Robert J. Weggel
Magnetic Field Design
MIT Magnet Lab · 2022–Present

BOARD

Priyanca Ford
Founder & CEO · Executive Board
2022–Present

Bandel Carano
Finance / Strategy
Oak Investment Partners / Stanford · 2025–2026

Patrick Schweiger
Fusion Device Engineering
Oklo / CFS / TerraPower · 2025–Present

SCIENTIFIC ADVISORS

Dr. Steven O. Dean
Fusion Policy & History
DOE / Fusion Power Associates · 2025–Present

Dr. Patrick H. Diamond
Plasma Turbulence & Transport
UC San Diego · 2025–Present

Dr. Jack J. Dongarra
HPC & Numerical Algorithms
Turing Award · 2025–Present

Dr. Nasr M. Ghoniem
Chief Material Scientist
UCLA · 2025–Present

Dr. Siegfried Glenzer
Plasma Physics & Laser Fusion
Stanford / SLAC · 2022–Present

Dr. David A. Hammer
Pulsed-Power Fusion
Cornell · 2025–Present

Dr. Donald A. Spong
Plasma Theory & Confinement
ORNL · 2025–Present

Dr. Curtis Smith
Risk Assessment & Nuclear PRA
MIT / Idaho National Lab · 2025–Present

RADM (Ret.) David Goggins
Naval Engineering & Power-Plant Design
U.S. Navy · 2023–2026

Dr. Konstantin Batygin
Mathematician
Caltech · 2022–2025

Dr. Ruben Fair
Magnet Design / ITER Liaison
PPPL / Jefferson Lab · 2022–2025

Dr. Paul S. Weiss
Materials & Nanotechnology
UCLA · 2022–2025

SCIENTIFIC AUDITORS

Dr. Wilfred A. Cooper
Plasma Equilibrium Theory
EPFL / Swiss Plasma Center · 2025–Present

Dr. Ahmed Hassanein
Plasma–Material Interactions
Purdue / Argonne · 2025–Present

Dr. Patrick E. Hopkins
Extreme Thermal Materials
U. of Virginia · 2025–Present

Dr. Peter Hosemann
Materials Joining & Structural Integrity
UC Berkeley · 2025–Present

Dr. Travis W. Knight
Advanced Nuclear Fuels & Systems
U. of South Carolina · 2025–Present

Dr. Philippe Lebrun
Cryogenics & Magnet Cooling
CERN · 2025–Present

Dr. Nitendra Singh
Nuclear Safety & Fuel Cycle
ITER · 2025–Present

Dr. Guido Van Oost
Magnetic Confinement & Fusion Systems
Ghent University · 2025–Present

Dr. Gary S. Was
Radiation Materials & Structural Integrity
U. of Michigan · 2025–Present

Dr. Ray Sedwick
Direct Energy Conversion
U. of Maryland · 2025

OPERATIONS

Michael Laughlin
Chief Operating Officer
2022–Present

Martin Owens
Chief Strategy Officer
LANL / GE Hitachi · 2022–Present

MG (Ret.) Paul Pardew
Chief Contracting Officer
Army Contracting Command · 2022–Present

David Beck
Fusion Commercialization
U.S. Space Force · 2024–Present

Sushma Bhatia
Environmental & Legislative
Google · 2022–Present

Michael De Frenza
Technology Licensing
2023–Present

MG (Ret.) Robin L. Fontes
Cybersecurity & Defense
Army Cyber Command · 2022–Present

Vijay Gehani
Supply Chain & Components
INOX India · 2024–Present

Jon Michel Greenwood
IT & AI Infrastructure
Live Nation · 2023–Present

Brian C. O'Neill
National Security
CIA / ODNI · 2022–Present

Gen. (Ret.) Gustave F. Perna
DoD Liaison
Operation Warp Speed · 2022–2023

Andrea Romero
Marketing Lead
2022–Present

Legal counsel is retained; those roles are held on the internal roster and are not listed here.

SOURCES

References

1 P I Ford, *Kronos Physics De-Risking Register (v8)*, Kronos Fusion Energy 2026 series, doi:10.5281/zenodo.22133057.

2 P I Ford, *AI and Quantum Computing for Fusion: ML Surrogates, Real-Time Control, and a Resource-Honest Quantum Frontier*, Kronos Fusion Energy 2026 series, doi:10.5281/zenodo.22645702. Official page: https://www.kronosfusionenergy.com/publications/ai-quantum-control.html.

3 P I Ford, *Resource-Honest Quantum Computing for Fusion: Variational Landau-Damping Emulation and ADAPT-VQE Low-Activation Alloy Chemistry Against the Classical Frontier*, Kronos Fusion Energy 2026 series, doi:10.5281/zenodo.22645718. Official page: https://www.kronosfusionenergy.com/publications/quantum-computing-for-fusion.html.

4 P I Ford, *First-Principles Near-Neutral Low-Activation Refractory Alloys for Fusion Plasma-Facing Components: Formation-Energy Screening and Entropy-Stabilized Composition-of-Matter Design*, Kronos Fusion Energy 2026 series, doi:10.5281/zenodo.22645744. Official page: https://www.kronosfusionenergy.com/publications/low-activation-alloys.html.

5 P I Ford, *A Tantalum- and Rhenium-Free Low-Activation Alloy Family for First Wall, Divertor and Direct-Energy-Converter Electrodes: A First-Principles Composition-of-Matter Study*, Kronos Fusion Energy 2026 series, doi:10.5281/zenodo.22645891. Official page: https://www.kronosfusionenergy.com/publications/a-tantalum-and-rhenium-free-low-activation-alloy-family.html.

6 P I Ford, *A Machine-Learning Interatomic-Potential to Activation-Transport Pipeline for Low-Activation Fusion Alloy Discovery: CHGNet Screening, DFT Confirmation, and OpenMC/FISPACT Down-Selection*, Kronos Fusion Energy 2026 series, doi:10.5281/zenodo.22645797. Official page: https://www.kronosfusionenergy.com/publications/ml-potential-materials-discovery-pipeline.html.

7 P I Ford, *First-Principles Radiation Tolerance of Centrepost REBCO in a Compact Spherical-Tokamak Breeder: Chain-Oxygen-Vacancy Formation by DFT+U and YBCO Displacement-Cascade Molecular Dynamics*, Kronos Fusion Energy 2026 series, doi:10.5281/zenodo.22645923. Official page: https://www.kronosfusionenergy.com/publications/first-principles-radiation-tolerance-of-centrepost-rebc.html.

8 A Peruzzo, J McClean, P Shadbolt, M-H Yung, X-Q Zhou, P J Love, A Aspuru-Guzik and J L O'Brien, *A variational eigenvalue solver on a photonic quantum processor*, Nat. Commun. **5**, 4213 (2014), doi:10.1038/ncomms5213.

9 H R Grimsley, S E Economou, E Barnes and N J Mayhall, *An adaptive variational algorithm for exact molecular simulations on a quantum computer*, Nat. Commun. **10**, 3007 (2019), doi:10.1038/s41467-019-10988-2.

10 H L Tang, V O Shkolnikov, G S Barron, H R Grimsley, N J Mayhall, E Barnes and S E Economou, *Qubit-ADAPT-VQE: an adaptive algorithm for constructing hardware-efficient ans\"atze on a quantum processor*, PRX Quantum **2**, 020310 (2021), doi:10.1103/PRXQuantum.2.020310.

11 A Kandala, A Mezzacapo, K Temme, M Takita, M Brink, J M Chow and J M Gambetta, *Hardware-efficient variational quantum eigensolver for small molecules and quantum magnets*, Nature **549**, 242 (2017), doi:10.1038/nature23879.

12 P J J O'Malley *et al.*, *Scalable quantum simulation of molecular energies*, Phys. Rev. X **6**, 031007 (2016), doi:10.1103/PhysRevX.6.031007.

13 J Romero, R Babbush, J R McClean, C Hempel, P J Love and A Aspuru-Guzik, *Strategies for quantum computing molecular energies using the unitary coupled cluster ansatz*, Quantum Sci. Technol. **4**, 014008 (2018), doi:10.1088/2058-9565/aad3e4.

14 I O Sokolov, P Kl Barkoutsos, P J Ollitrault, D Greenberg, J Rice, M Pistoia and I Tavernelli, *Quantum orbital-optimized unitary coupled cluster methods in the strongly correlated regime: can quantum algorithms outperform their classical equivalents?*, J. Chem. Phys. **152**, 124107 (2020), doi:10.1063/1.5141835.

15 J Tilly, H Chen, S Cao, D Picozzi, K Setia, Y Li, E Grant, L Wossnig, I Rungger, G H Booth and J Tennyson, *The variational quantum eigensolver: a review of methods and best practices*, Phys. Rep. **986**, 1 (2022), doi:10.1016/j.physrep.2022.08.003.

16 S McArdle, S Endo, A Aspuru-Guzik, S C Benjamin and X Yuan, *Quantum computational chemistry*, Rev. Mod. Phys. **92**, 015003 (2020), doi:10.1103/RevModPhys.92.015003.

17 A Aspuru-Guzik, A D Dutoi, P J Love and M Head-Gordon, *Simulated quantum computation of molecular energies*, Science **309**, 1704 (2005), doi:10.1126/science.1113479.

18 J R McClean, S Boixo, V N Smelyanskiy, R Babbush and H Neven, *Barren plateaus in quantum neural network training landscapes*, Nat. Commun. **9**, 4812 (2018), doi:10.1038/s41467-018-07090-4.

19 S B Bravyi and A Yu Kitaev, *Fermionic quantum computation*, Ann. Phys. **298**, 210 (2002), doi:10.1006/aphy.2002.6254.

20 J T Seeley, M J Richard and P J Love, *The Bravyi-Kitaev transformation for quantum computation of electronic structure*, J. Chem. Phys. **137**, 224109 (2012), doi:10.1063/1.4768229.

21 R Babbush, C Gidney, D W Berry, N Wiebe, J McClean, A Paler, A Fowler and H Neven, *Encoding electronic spectra in quantum circuits with linear T complexity*, Phys. Rev. X **8**, 041015 (2018), doi:10.1103/PhysRevX.8.041015.

22 M Reiher, N Wiebe, K M Svore, D Wecker and M Troyer, *Elucidating reaction mechanisms on quantum computers*, Proc. Natl. Acad. Sci. USA **114**, 7555 (2017), doi:10.1073/pnas.1619152114.

23 V von Burg, G H Low, T H\"aner, D S Steiger, M Reiher, M Roetteler and M Troyer, *Quantum computing enhanced computational catalysis*, Phys. Rev. Research **3**, 033055 (2021), doi:10.1103/PhysRevResearch.3.033055.

24 J Lee, D W Berry, C Gidney, W J Huggins, J R McClean, N Wiebe and R Babbush, *Even more efficient quantum computations of chemistry through tensor hypercontraction*, PRX Quantum **2**, 030305 (2021), doi:10.1103/PRXQuantum.2.030305.

25 J J Goings, A White, J Lee, C S Tautermann, M Degroote, C Gidney, T Shiozaki, R Babbush and N C Rubin, *Reliably assessing the electronic structure of cytochrome P450 on today's classical computers and tomorrow's quantum computers*, Proc. Natl. Acad. Sci. USA **119**, e2203533119 (2022), doi:10.1073/pnas.2203533119.

26 P Hohenberg and W Kohn, *Inhomogeneous electron gas*, Phys. Rev. **136**, B864 (1964), doi:10.1103/PhysRev.136.B864.

27 W Kohn and L J Sham, *Self-consistent equations including exchange and correlation effects*, Phys. Rev. **140**, A1133 (1965), doi:10.1103/PhysRev.140.A1133.

28 J P Perdew, K Burke and M Ernzerhof, *Generalized gradient approximation made simple*, Phys. Rev. Lett. **77**, 3865 (1996), doi:10.1103/PhysRevLett.77.3865.

29 V I Anisimov, J Zaanen and O K Andersen, *Band theory and Mott insulators: Hubbard U instead of Stoner I*, Phys. Rev. B **44**, 943 (1991), doi:10.1103/PhysRevB.44.943.

30 S L Dudarev, G A Botton, S Y Savrasov, C J Humphreys and A P Sutton, *Electron-energy-loss spectra and the structural stability of nickel oxide: an LSDA+U study*, Phys. Rev. B **57**, 1505 (1998), doi:10.1103/PhysRevB.57.1505.

31 A J Cohen, P Mori-S\'anchez and W Yang, *Insights into current limitations of density functional theory*, Science **321**, 792 (2008), doi:10.1126/science.1158722.

32 C J Cramer and D G Truhlar, *Density functional theory for transition metals and transition metal chemistry*, Phys. Chem. Chem. Phys. **11**, 10757 (2009), doi:10.1039/b907148b.

33 R J Bartlett and M Musia, *Coupled-cluster theory in quantum chemistry*, Rev. Mod. Phys. **79**, 291 (2007), doi:10.1103/RevModPhys.79.291.

34 Q Sun *et al.*, *Recent developments in the PySCF program package*, J. Chem. Phys. **153**, 024109 (2020), doi:10.1063/5.0006074.

35 S J Zinkle and G S Was, *Materials challenges in nuclear energy*, Acta Mater. **61**, 735 (2013), doi:10.1016/j.actamat.2012.11.004.

36 J Knaster, A Moeslang and T Muroga, *Materials research for fusion*, Nat. Phys. **12**, 424 (2016), doi:10.1038/nphys3735.

37 J-W Yeh, S-K Chen, S-J Lin, J-Y Gan, T-S Chin, T-T Shun, C-H Tsau and S-Y Chang, *Nanostructured high-entropy alloys with multiple principal elements: novel alloy design concepts and outcomes*, Adv. Eng. Mater. **6**, 299 (2004), doi:10.1002/adem.200300567.

38 J E Menard *et al.*, *Fusion nuclear science facilities and pilot plants based on the spherical tokamak*, Nucl. Fusion **56**, 106023 (2016), doi:10.1088/0029-5515/56/10/106023.

39 B N Sorbom *et al.*, *ARC: a compact, high-field, fusion nuclear science facility and demonstration power plant with demountable magnets*, Fusion Eng. Des. **100**, 378 (2015), doi:10.1016/j.fusengdes.2015.07.008.

COLOPHON

How this document was made

The Kronos Fleet — Combined Editorial, 2026 is set in **Fraunces** (display), **Gelasio** (text), and **IBM Plex Mono** (data & equations), carried forward from the Kronos editorial design system.

The figures are rendered at 300 dpi from the deposited generator scripts; the document is composed as a single self-contained file with embedded fonts and imagery, paginated to US Letter, and rendered to PDF through a headless Chromium engine in matched light and dark editions.

Every headline quantity carries an evidence class; withdrawn and restated values are marked as such. Nothing herein is frozen beyond the founder-approved Tier-A set.

Explore it live — turn the interactive 3-D model, run the deposited solvers in the physics validator, and watch the companion film series.

LEGAL NOTICE

Notice, status, and distribution

Conceptual design & simulation study. This document reports a conceptual design and simulation study. It is not a construction commitment, a safety-analysis report, a regulatory filing, or an offer of securities. Forward-looking statements — schedules, costs, market sizes, and performance — are estimates subject to the limitations set out in the Simulations part and may change.

Numbers and their classes. Quantities are reported with evidence classes and case labels; modelled, assumed, and requirement-class values are identified as such and are not to be quoted without their labels.

Public edition. This edition carries the physics and design only; all financial, funding, and defense-commercial content has been removed for public distribution. The scientific text corresponds to the arXiv and journal submissions.

© 2026 Kronos Fusion Energy. All rights reserved. Hyperion, Aegis, and MetroVolt are product designations of Kronos Fusion Energy.

THE 2026 KRONOS SERIES

One programme, many papers

This editorial is one paper in the Kronos 2026 series — a real fusion company's complete, reproducible physics record for a spherical-tokamak breeder and its low-neutron D–^{3}He tandem-mirror burners. Every headline number is a frozen anchor in the Physics De-Risking Register.

Explore the whole programme: the De-Risking Register, the interactive 3-D model, and the physics validator.

KRONOS FUSION ENERGY

Quantum Chemistry Beyond DFT for Low-Activation Fusion Alloys: ADAPT-VQE Correlation Energies for Composition-of-Matter Screening with Fault-Tolerant Resource Estimates

A real fusion company building real machines. Explore the science, live.

Zenodo · doi:10.5281/zenodo.22645929

Read on kronosfusionenergy.com

The Physics De-Risking Register

© 2026 KRONOS FUSION ENERGY · FAMILY-OWNED AMERICAN COMPANY